Icarus 226 (2013) 629–640

Contents lists available at SciVerse ScienceDirect

Icarus

journal homepage: www.elsevier.com/locate/icarus

Shape model and surface properties of the OSIRIS-REx target Asteroid (101955) Bennu from radar and lightcurve observations

Michael C. Nolan [a,*], Christopher Magri [b], Ellen S. Howell [a], Lance A.M. Benner [c], Jon D. Giorgini [c], Carl W. Hergenrother [d], R. Scott Hudson [e], Dante S. Lauretta [d], Jean-Luc Margot [f], Steven J. Ostro [c,1], Daniel J. Scheeres [g]

[a] Arecibo Observatory, HC 3 Box 53995, Arecibo, PR 00612, USA
[b] University of Maine at Farmington, 173 High St, Preble Hall, Farmington, ME 04938, USA
[c] Jet Propulsion Laboratory, California Institute of Technology, Pasadena, CA 91109, USA
[d] Lunar and Planetary Laboratory, University of Arizona, Tucson, AZ 85721, USA
[e] Washington State University, Tri-Cities, Richland, WA 99354, USA
[f] Department of Earth and Space Sciences, University of California, Los Angeles, CA 90295, USA
[g] University of Colorado at Boulder, 429 UCB, Boulder, CO 80309-0429, USA

ARTICLE INFO

Article history:
Received 7 February 2013
Revised 14 May 2013
Accepted 14 May 2013
Available online 22 June 2013

Keywords:
Radar observations
Asteroids, Surfaces
Asteroids, Rotation
Asteroid Bennu

ABSTRACT

We determine the three-dimensional shape of near-Earth Asteroid (101955) Bennu based on radar images and optical lightcurves. Bennu was observed both in 1999 at its discovery apparition, and in 2005 using the 12.6-cm radar at the Arecibo Observatory and the 3.5-cm radar at the Goldstone tracking station. Data obtained in both apparitions were used to construct a shape model of this object. Observations were also obtained at many other wavelengths to characterize this object, some of which were used to further constrain the shape modeling. The lightcurve data, along with an initial determination of the rotation period derived from them, simplified and improved the shape modeling.

Below we briefly describe the observations and shape modeling process. We discuss the shape model and the implications for the possible formation and evolution of this object. We also describe the importance and limitations of the shape model in view of the fact that this object is the target of the OSIRIS-REx spacecraft mission.

1. Introduction to Bennu

Asteroid (101955) Bennu was discovered in September 1999 by the LINEAR survey and designated 1999 RQ_{36}. It is an Apollo Near-Earth Object (NEO) with a semi-major axis of 1.126 AU, an eccentricity of 0.205 and an orbital inclination of 6°.

Bennu is a B-type asteroid characterized by a linear, featureless spectrum with bluish to neutral slope at visible wavelengths. Spectral analysis suggests that the most likely meteorite analogs for Bennu are the CI or CM meteorites (Clark et al., 2011). Near-infrared spectroscopic data show evidence of a thermal tail longward of 2 μm, suggesting a very low albedo (0.035 ± 0.015) that is consistent with a carbonaceous surface. Thermal infrared data show that there is no observable dust or gas in the proximity of Bennu. Dynamical and spectral analyses suggest that Bennu may be a liberated member of the Polana asteroid family (Campins et al., 2010) or the related Eulalia family (Walsh et al., 2012).

Bennu is the primary target of the OSIRIS-REx Asteroid Sample Return Mission, selected by NASA as the third New Frontiers mission in May 2011. OSIRIS-REx will thoroughly characterize near-Earth asteroid Bennu. This asteroid is both the most accessible carbonaceous asteroid and one of the most potentially hazardous asteroids known (Milani et al., 2009). The information obtained from radar characterization of this asteroid was critical in mission target selection and supports OSIRIS-REx science definition and mission planning.

2. Observations

Bennu is in a pseudo-resonance with the Earth, and makes close passes about every 6 years, though at varying distances. It has been observed at every apparition since its discovery. The radar observations with Arecibo and the Goldstone planetary radar systems were carried out shortly after discovery, from 21 to 25 September, 1999, and again from 16 September to 2 October in 2005 (Table 1). Further radar observations obtained in September 2011 had too low a signal-to-noise ratio (SNR) to be useful for characterizing the shape of the asteroid. Chesley et al. (2013) used them, along

* Corresponding author.
E-mail address: nolan@naic.edu (M.C. Nolan).
[1] Deceased.

0019-1035/$ - see front matter © 2013 Elsevier Inc. All rights reserved.
http://dx.doi.org/10.1016/j.icarus.2013.05.028

Table 1
Observation dates and circumstances. The complete list of radar observations is given in online Supplementary Table S1. R is heliocentric distance. Δ is geocentric distance. Arecibo (A) and Goldstone (G) observatories obtained radar observations, the others are optical lightcurves obtained at the Catalina Station 1.5-m telescope (B) and the Chuguev Observation Station 0.7-m telescope (C). The Arecibo radar images in 1999 were taken at 15-m (100 ns) resolution because the 7.5-m (50 ns) resolution capability was not yet available. The tabulated sub-Earth latitude adopts the model pole at ecliptic latitude and longitude (−88°, 45°). The 19-m (125 ns) data are from Goldstone, and have much lower SNR than the rest of the radar data, which are from Arecibo. They are included because they cover viewing geometries not seen from Arecibo. The data marked with a * on the observatory are not included in the fits due to insufficient SNR and/or resolution for modeling, but are tabulated here for completeness. The 1999 lightcurves are from Krugly et al. (2002). The 2005 lightcurves are described in Hergenrother et al. (2013).

UT date	UT time	R (AU)	Δ (AU)	Observatory	Solar phase (°)	Image resolution (m)	Sub-Earth latitude (°)
1999 09 20		1.013	0.018	C	62		−32
1999 09 21		1.010	0.016	C	70		−28
1999 09 21	08:54–14:30	1.010	0.016	G*		19	−28
1999 09 22		1.006	0.015	C	81		−22
1999 09 23	09:18–14:30	1.002	0.015	G		19	−11
1999 09 23	09:40–11:29	1.002	0.015	A		15	−11
1999 09 24	10:20–11:57	0.999	0.016	A		15	−3
1999 09 25	11:03–13:00	0.996	0.018	A		15	+4
1999 09 25	18:43–19:12	0.995	0.018	G		19	+6
1999 10 01	12:56–14:05	0.979	0.034	G*		19	
2005 09 14		1.026	0.041	B	60		−26
2005 09 15		1.022	0.039	B	63		−24
2005 09 16		1.019	0.037	B	67		−22
2005 09 16	08:36–09:31	1.019	0.037	A		7.5	−22
2005 09 17		1.016	0.035	B	71		−20
2005 09 18	11:09–13:41	1.013	0.034	G		19	−16
2005 09 19	11:05–14:27	1.009	0.033	G		19	−13
2005 09 20	09:04–11:30	1.006	0.033	A		7.5	−10
2005 09 28	11:53–13:40	0.981	0.046	A		7.5	+13
2005 10 02	12:51–14:15	0.970	0.058	A		7.5	+18
2011 09 27		0.962	0.197	A*		300	
2011 09 28		0.960	0.200	A*		300	
2011 09 29		0.957	0.202	A*		300	

with the other observations reported here, for computing its orbit. The observations at Goldstone have lower (by a factor of about 20) SNR than the Arecibo images, but many were obtained at times when the object was not visible from Arecibo. No further ground-based radar observations will be possible until 2037 with existing facilities. Some additional optical observations may be possible in 2017, though it will be quite faint, $M_V = 20$, making detailed studies difficult.

The circumstances of the observations are listed in Table 1. Radar data were obtained and processed using standard techniques (Magri et al., 2007). A monochromatic circularly-polarized signal is transmitted, and the reflected echo is received in both circular polarizations, referred to as the OC ("opposite circular" to the transmitted circular polarization) and SC ("same-circular" to the transmitted circular polarization). For some of the imaging observations, data-rate limitations prevented us from recording both polarizations, so only the brighter OC echoes were recorded.

The total energy received depends upon the reflectivity of the surface material and its orientation with respect to the observer. The distribution of energy in the two orthogonal polarizations gives an estimate of the surface roughness, or the amount of light multiply scattered compared to that returned by specular reflectance. Other compositional factors may also influence the polarization ratio (Benner et al., 2008; Magri et al., 2001). Ephemeris improvements are routinely made for all asteroids observed with radar. The shape modeling was done using the brighter OC sense data (delay-Doppler images and Doppler spectra).

A delay-Doppler image is a measure of the object's extent in the line-of-sight and its instantaneous velocity dispersion from its own rotation (in the reference frame of the observer). The absolute range and orbital velocity are measured and used to refine the orbit, but are removed in the shape modeling process. The two axes are independent and unrelated in spatial resolution. Each image pixel is a combination of contributions from any area of the surface that has the same distance and line-of-sight velocity from the observer, which is generally two locations on a convex object (the "north–south ambiguity") and can be more than two on an irregular object (Ostro et al., 2002). In the shape modeling, synthetic radar images (or lightcurve points) are computed from the shape and compared to the observations. The shape is then adjusted to improve the fit between the synthetic images and the observations. The radar scattering is modeled to depend on the incidence angle θ as a function of the form $d\sigma/dA = R(C+1)\cos^{2C}\theta$ (Mitchell et al., 1996), where R and C are fit parameters. Examples of delay-Doppler images of Bennu are shown in the first column of the panels in Fig. 1. The asteroid's motion in the sky changes the viewing geometry both within a day and between days, so that it is possible to solve for the pole orientation and object shape. If the coverage is extensive enough, the ambiguities within each image can be resolved, and a unique shape can be derived for the asteroid. It is common that ambiguities can only be partially resolved, so that, for example, a feature can be identified and located in latitude and longitude, but not whether the latitude is positive or negative. The details of this iterative, non-linear inverse-modeling process are given in Magri et al. (2007) based on the method of Hudson (1993). Because of the pseudo-resonance in the orbit, the viewing geometry is similar every 6 years. The coverage was more extensive in 2005 than in 1999, but at lower SNR, since the asteroid was farther away. The viewing geometry was always near the equator (−16° to +18° for the radar data, slightly wider for the lightcurve observations), so the polar regions are not as well observed as the equatorial ones.

Fig. 1 shows a sample of the radar images and model fits. The complete set of data and fits used in the modeling are shown in Supplementary online Fig. S1. In each row the observed radar image is in the first column on the left, the synthetic radar image generated from the model shape is in the center column, and the plane-of-sky view of the model shape as it would appear from the Earth is in the right column. The difference between the model radar image and the observed image is calculated and summed for each image in the data set to obtain the χ^2 value. Weights are used to guide the modeling process, based on differences in the data quality and the type of data used. The actual "objective function"

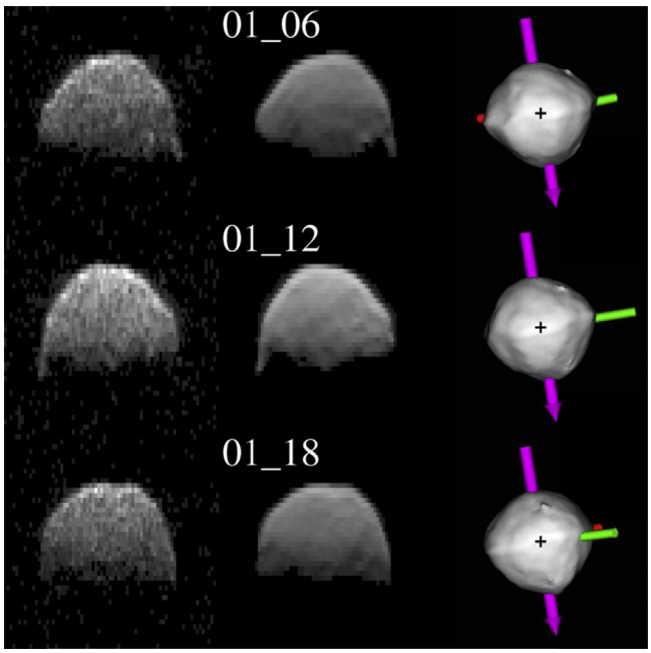

Fig. 1. Sample of radar images and the model on 1999 September 24. The left column shows the radar data. The center column shows the model fit to the data. The right column shows the model as it would appear on the sky. In the radar frames, the observer is at the top of the frame looking down. The vertical scale is range from the observer in units of 100 ns, or 15 m. The horizontal axis is Doppler shift, or rotation velocity, which, for a solid body, corresponds to linear distance from the rotation axis after projection onto the plane of the sky, and has been scaled to give approximately square pixels. The numbers label the data sets as described in Supplementary online Table S1. The complete set of data and fits are shown in the Supplementary online Fig. S1.

that is minimized is a sum of the reduced χ^2 and a set of "penalty functions" that push the model to have "reasonable" behavior, such as enforcing principal-axis rotation and suppressing extreme shapes. We will generally refer to the objective function as simply χ^2, except where the distinction is relevant.

By visually examining the raw radar images, it is clear that Bennu is roughly spheroidal with some large-scale but fairly subtle surface features. In the images from 1999, the terminator is clearly discernible due to their very high SNR. The visible extent of those images is about 15–20 pixels, or 225–300 m, and the illuminated area is roughly hemispherical. Thus an initial rough estimate of the diameter is 450–600 m. The Doppler bandwidth is 4 Hz for the Arecibo frequency of 2380 MHz, which for this diameter lets us estimate that the rotation period is about 4 h. It could be shorter if the viewing geometry is not equatorial, but the shape does not appear to repeat in the ~2.5-h Arecibo viewing window on 1 day. The line-of-sight extent and bandwidth do not vary by more than 15% either within a day or between days, which indicates that the average values are good estimates of the size and apparent rotation rate.

3. Shape modeling

3.1. Variable SNR

Because Bennu was closer to the Earth during the 1999 apparition, those data had very high signal level compared to the thermal background, SNR > 10 per pixel even at the terminator. However, there were only 3 days of observation, and the radar datataking system was not yet capable of operation at the 7.5-m resolution that was achieved in 2005. The 1999 data were also dominated by "self-noise" or "fading", where the thermal noise is chi-squared distributed (that, is, much "spikier" than a Gaussian noise distribution) and an additional Rayleigh-distributed noise source is present due to the signal itself, which is proportional to the signal intensity (Elachi, 1987; Ulabi et al., 1982). As a result, it was necessary to weight the data carefully. The very bright specular echo (Fig. 2a) from the subradar point of the target had a signal ~300 times the thermal noise, but nearly the same actual SNR as the much fainter terminator region needed to provide the size information. To solve this problem, we developed an intra-image weighting scheme that weighted different parts of individual images depending on the true SNR. The difficulty in doing that is that the only way to determine the standard deviation of the data is by examining those same data. Since the SNR is low, these data vary by a factor of several. If one naively assumes a constant SNR throughout the image, one determines a larger weight for points that happen to be low, artificially biasing the results. In addition, since the brightest points are from noisy data, the model tends to be dominated by the few 1999 images, ignoring the 2005 data.

In order to compute a weight mask, we averaged together all of the data from each day, improving the SNR by a factor of $\sqrt{N}$, but discarding much of the shape information. We used this sum to compute the average signal power as a function of position in the radar image, and computed the variance due to thermal and self-noise expected if the true echo power were that in the average image. We then used these "variance images" to weight the data. Within 1 day, a single mask was used, shifted in delay-Doppler space as necessary to align with the data. This shift accounts for imperfections in the observing ephemeris and is estimated as part of the shape modeling process, which must therefore be carried out in two stages, first crudely without weighting masks and then in refined fashion with properly shifted masks.

The fits to the 1999 data thus fit both the leading edge and the terminator, which constrained the size and Doppler broadening well, without losing the higher resolution and more complete sky coverage of the 2005 data. This procedure worked well, at least in part because the object is symmetrical enough that the shape of the necessary weight mask does not change significantly over the daily observation window. For more asymmetric shapes, it would be necessary to be more careful in generating the masks. Possibilities include use of a shorter averaging interval, using a low-fidelity model instead of the data, adding a spatial smoothing to the temporal smoothing described here, using the lower-contrast "SC" images, or various combinations of those methods.

3.2. Pole determination

One of the reasons that the shape modeling of Bennu is so successful is that high-quality lightcurves were obtained (see Hergenrother et al., 2013) so that the rotation period was well-constrained independent of the radar imaging. In the simplest case, a spherical object, the observations of line-of-sight velocities translate directly into distances from the rotation axis once the rotation period is known. Thus the orientation of the axis with respect to the line of sight is also determined if the rotation period is known independently. However, the orientation of the axis in the plane of the sky is always undetermined in a single radar image, and must be determined from the whole set of images and the object's motion over the entire period of observation. More irregular shapes complicate this procedure, and an iterative determination of shape and pole is generally necessary unless other data are available to further constrain the pole, such as the speckle-tracking method of Busch et al. (2011). Two separate apparitions usually help enormously to determine the pole orientation (e.g., Ostro et al., 2006), unless they happen to have nearly the same viewing geometry.

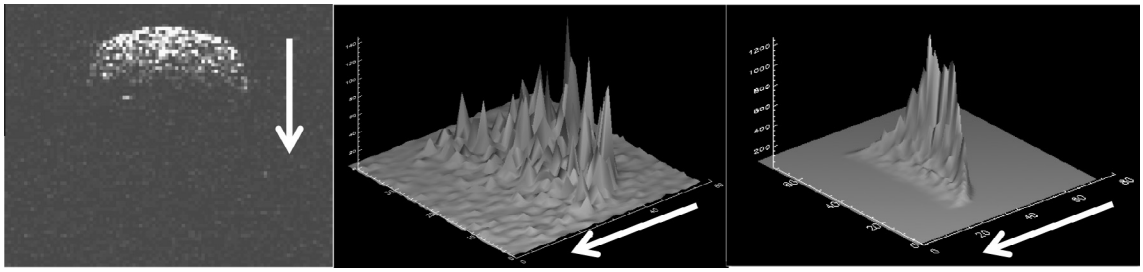

Fig. 2. White arrows show direction of increasing range. A single delay-Doppler image (left) can have a high SNR compared to the thermal background, but as shown in surface plot of signal power (center), is spiky due to self-noise. In any one pixel, the best estimate of the self-noise in that pixel is its own intensity, but this value is clearly poorly determined. We can sum images to improve the SNR, but then the resulting sum is smeared due to target rotation. By averaging all of the images within a day, we discard much of the shape information, but are able to compute the mean intensity at that delay-Doppler position, which is the information we need to estimate the true SNR. We then variance-weighted the data using a weighting mask that is the reciprocal of the image (right), which is the square of the mean image.

In order to determine the pole, we performed a grid search of possible poles and looked at the χ^2 goodness of fit for all the images used. The shape is also allowed to change so some initial models are required to get a general range of possible shapes and dimensions. The shape is first modeled as a triaxial ellipsoid, and then a smooth set of spherical harmonic functions, and finally an arbitrary set of approximately equal-sized triangular facets (also called "vertex" or "plate" models). The grid of pole positions reveals general regions that are allowed or not for reasonable ranges of object shapes. For a spherical body, the diameter can be measured from the range extent in the images. If the rotation rate is also known, then the rotational Doppler broadening determines the inclination of the pole to the line of sight, giving a pair (prograde/retrograde) of circles of possible pole orientations. If the observation is repeated with different viewing geometries, the intersection of these circles will give a unique pole direction, though with an unknown sign (Magnusson et al., 1989). For more general shapes, the range depth observed in one image is not the same as the edge-to-edge distance that determines the bandwidth, so the allowed "circles" become bands, and more observations are required to determine the pole.

As seen in Fig. 1, the radar images of Bennu appear nearly semicircular, suggesting a roughly spherical object. We therefore began our modeling by assuming a triaxial ellipsoid, using only the radar images and optical lightcurves from 2005. In order to speed the process and increase the SNR of the data, we summed the radar images into 10-min averages, or about 15° of rotation. We fixed the rotation period at 4.290 h, as initially determined from lightcurves (Hergenrother et al., 2013). The best χ^2 was achieved with pole orientations at mid-latitudes.

Visually comparing the data with the model images (Fig. 3), it appears that the leading edges of the data are fairly well modeled, but the terminator region less so. Also, because the terminator region is faint, it is difficult to determine the size of the target. We next added in the photometric lightcurve data from 2005 to the model constraints and allowed the period to vary slightly to allow for the small difference between the sidereal rotation period used in modeling and the synodic period observed at the telescope: the apparent rotation due to changing observation and illumination geometry over the 4-day observing interval is small but measurable. The lightcurve data are included in the same way as the radar data: synthetic lightcurves are computed from the shape model and compared to the data. The preferred poles remained at mid-latitudes, but with the lightcurve data included the retrograde pole is preferred. This occurs because the rate of sky motion changed over the course of the observation, giving a phase shift to the observed lightcurve, making it possible to distinguish rotation in the same or opposite direction as the sky motion. We proceeded to increase the model complexity to a set of spherical harmonics of degree and order 8 (approximately the same resolution as the rotational smearing due to the summing described above), and also to include the 1999 data to better constrain the size and choose among the possible pole orientations. Increasing the order of the shape dramatically changed the pole solutions: the best solution became one nearly-retrograde solution and one (less preferred) nearly equatorial one. This extreme difference in pole solutions between the ellipsoid model and the more complex one was surprising, and we believe it is due to the ridged shape of Bennu. The equatorial diameter is substantially (>10%) larger than the "average" diameter, and as a result, the limb-to-limb distance that determines the bandwidth is not in general the same as the range depth, which is not well-represented by an ellipsoid shape (Busch et al., 2011).

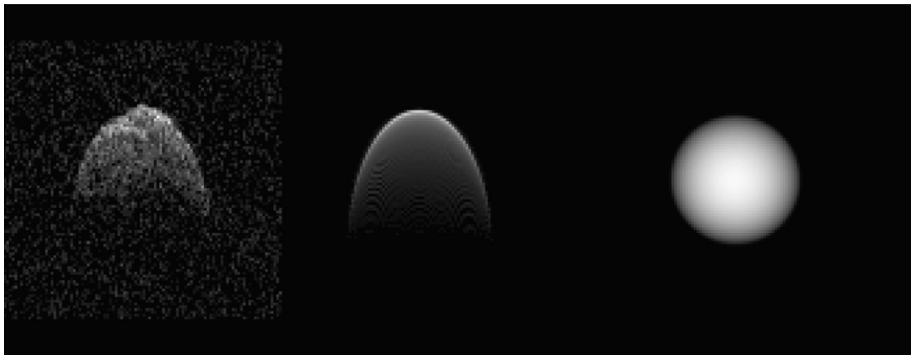

Fig. 3. Data (left), simulated data (center) and plane-of-sky image for one of the best-fit triaxial ellipsoid poles. Note that the shape of the leading edge is fairly well matched by the model, but the terminator is too far back in the model.

The final improvement to the global pole solution came when we included both the 1999 and 2005 radar and lightcurve data simultaneously. The 2005 data have better aspect coverage, but the 1999 data have higher SNR. The uncertainty in the rotation period from the 2005 lightcurve measurements was 0.004 h, or about 10 full rotations measurement uncertainty plus the sidereal/synodic difference of about 30 rotations over the 6-year interval between the 1999 and 2005 apparitions, which complicated the use of both data sets simultaneously. To address this difficulty, we chose a nominal rotation rate within the uncertainty, and searched a grid of possible poles allowing the period to float over a narrow range so that it would "lock in" an acceptable (though not necessarily correct) number of complete rotations with the viewing aspect the same in the two observing windows. For each trial pole, we performed an ellipsoid fit to get the basic shape with the long axis in the right direction. Since an ellipsoid is bilaterally symmetric, we then performed two 8th order spherical-harmonic fits—one with the best-fit ellipsoid and the other with the period changed to give an extra half-rotation between 1999 and 2005. The output of this search was a map of χ^2 space (shown in Fig. 4) that showed that the retrograde pole near ecliptic latitude −90° was strongly preferred, and the mid-latitude solution disappeared. These runs however demonstrated a complication with the modeling: Bennu was much closer in 1999 than in 2005, so that the noise statistics were very different in the 2 years, as discussed in Section 3.1.

3.3. Faceted models

With good constraints on the pole and rotation period, we proceeded to refine the shape. The best spherical harmonic solutions were converted to faceted "plate model" or "vertex" shapes and the shape further refined. The faceted model was generated by sampling the spherical harmonic model at 1148 approximately equal-spaced vertices, giving a horizontal resolution of about 25 m between vertices. We reduced the number of images summed to 6° of asteroid rotation—25 m at the equator, to match the model resolution. We then refined this model. We chose a set of rotation poles near the result from the spherical harmonic fitting and allowed the model to iterate. There are a number of smoothing parameters and physical constraints imposed on the model. We chose parameters that enforce a uniform mass distribution and principal-axis rotation. After some experimentation, we chose a set of smoothing parameters that allowed the shape to evolve but did not result in spiky artifacts related to features not evident in the data. An interesting topographical feature, possibly a boulder, was seen in the raw radar images. The resolution of the model was increased in the region of the boulder to 5 m by adding 100 extra vertices in each hemisphere near the position of the feature so that the model could represent it. We do not expect accurate details of the boulder, as the data images are smoothed to about 18 m resolution at that latitude.

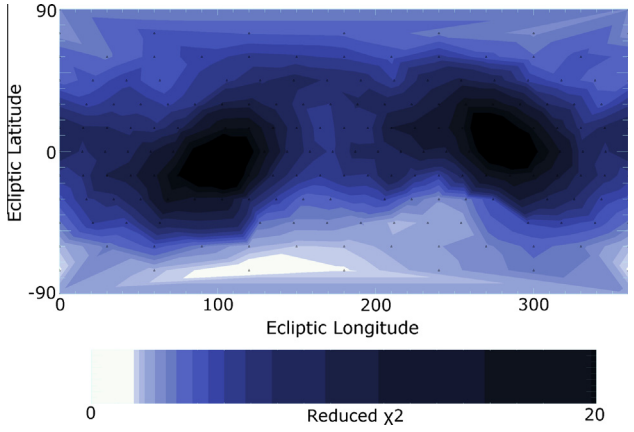

Fig. 4. Map of χ^2 with pole orientation using the combined 1999 and 2005 data set and an 8th order spherical harmonic shape. Triangles show the poles for individual model runs. Black regions have the highest χ^2 (poorest fit) and white regions the lowest. The two large dark areas show that the regions where the line of sight lies nearly along the pole are "forbidden", because the Doppler bandwidth would change dramatically with viewing angle, which is not observed. The north–south ambiguity intrinsic to radar observations is broken due to the motion of the target with respect to the Earth. The pole solution near ecliptic latitude −90 is clearly favored. Further studies examined only poles near this one.

The rotation rate and pole direction of Bennu were further refined using a smaller grid-search near the best-fit values from the earlier modeling. A grid search of the pole position at 5° spacing showed that the pole direction is within 15° of ecliptic latitude −90°. Using this pole and several nearby for comparison, a grid search of rotation rate showed a minimum at 4.297461 h, with a comb of solutions spaced by 0.000352 h corresponding to integer numbers of rotations over the 6-year observation interval. The simple fit of the χ^2 due to the lightcurve as a function of rotation rate suggests an uncertainty of ±5 rotations. Thus our preferred sidereal period is 4.29746 ± 0.002 h, which is actually a choice of one of eleven periods each individually uncertain to 0.00002 h.

With the rotation rate refined, we performed a finer grid search on the pole position, resulting in a best-fit pole with ecliptic coordinates $\beta = -88°$, $\lambda = 45°$ and an uncertainty of 5°. This search was performed with the full-resolution plate model shape allowed to float to avoid having a fixed shape force the rotation pole to match features in the radar images.

The best-fit shape is shown in Fig. 5, projected along the three principal axes. There does seem to be some north–south symmetry in surface features. Because of the nearly-equatorial viewing geometry, this is an artifact of the radar data, and the varying degree of symmetry in different parts of the object may result from variable rotational coverage. The volume derived is 0.062 km^3 ± 10%, with the error dominated by the large uncertainty in the Z-axis dimension. A sphere with the apparent average range extent in the radar images has a volume of 0.078 km^3, a 25% error. Note that when determining a size from extents or areas, a sphere always overestimates the volume compared to any real shape, which has been noted (A. Harris, personal communication) to contribute to a systematic underestimate of densities of objects in binary systems whenever the shapes are not known.

The best-fit axes and uncertainties are given in Table 2. The overall shape and features are well-determined and consistent between the two apparitions. Bright regions in the radar images indicate surface features, although a contribution by different reflectance properties in different surface materials cannot be ruled out. The spectral uniformity does not support large scale compositional differences. Small scale differences, such as exposure of fresh materials in the bottom of a crater, might also be accompanied by topographical features in a radar image. The overall shape of Bennu is similar to that of 1999 KW$_4$ and other binary near-Earth asteroids despite the slower rotation rate and lack of a satellite. This result is not unprecedented: 2008 EV$_5$ has a similar shape and also does not have a detected satellite (Busch et al., 2011). The smooth equatorial region and sloped regions towards the poles may be affected by migration of loose material in a similar way, only without the additional tidal effects of a satellite. Or perhaps a satellite was present at some time in the past, and has since been lost. In any case, the spheroidal shape in such a small object suggests a loose rubble-pile internal structure with little or no internal strength, and that the spin rate has been (or is being) altered, probably due to the YORP effect (Vokrouhlický et al., 2003). On-going surface migration might be observed by the OSIRIS-REx cameras.

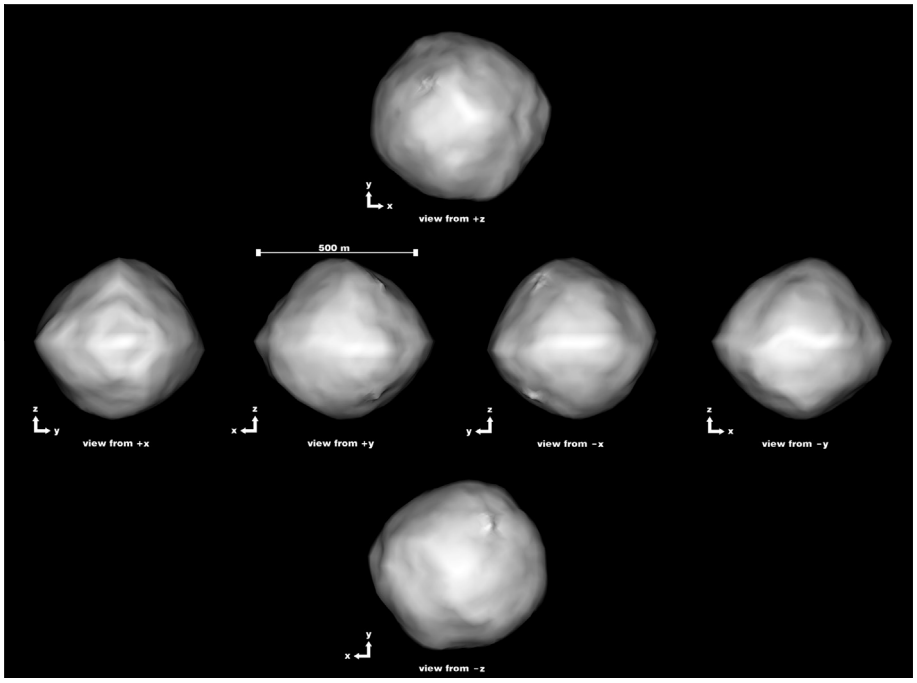

Fig. 5. The shape of Bennu showing the views along the principal axes. Some of the apparent north–south symmetry is a model artifact from the near-equatorial viewing geometry. The "boulder" feature is actually in the southern hemisphere.

Table 2
Properties of Bennu determined from the observations in this paper. Uncertainties reported are 1-sigma, but for the shape parameters are conservative and somewhat subjective. The uncertainties in the radar cross-sections are almost entirely due to calibration uncertainty, taken to be 25%. The calibration errors largely cancel in the polarization ratio computation, and the uncertainties shown reflect day-to-day variability rather than measurement uncertainty.

Mean diameter	492 ± 20 m
Projected area at equatorial viewing aspect	0.191 ± 0.006 km^2, 493 m equivalent diameter
Long and intermediate axes	565, 535 ± 10 m
Polar diameter	508 ± 52 m
Volume, V	0.0623 ± 0.006 km^3
Surface area, A	0.786 ± 0.04 km^2
12.6-cm OC radar cross section, σ_{OC}	0.023 ± 0.006 km^2
12.6-cm SC radar cross-section, σ_{SC}	0.0043 ± 0.001 km^2
12.6-cm circular polarization ratio, μ_C	0.18 ± 0.03
OC radar scattering dependence on incidence angle	$\cos^{1.18}\theta$
3.5-cm OC radar cross-section, σ_{OC}	0.034 ± 0.012 km^2
3.5-cm SC radar cross-section, σ_{SC}	0.0068 ± 0.0024 km^2
3.5-cm circular polarization ratio, μ_C	0.19 ± 0.03
Sidereal rotation period	4.29746 ± 0.002 h
Pole orientation (ecliptic coordinates)	(−88°, 45°) ± 4° (great circle)
Flattening	4 ± 8%

3.4. Uncertainties

The uncertainties were determined by running suites of models varying the parameter to be tested and also varying (or floating) the parameters that are most likely to have high covariance with those parameters. We then looked at the resulting χ^2 values and also the raw model fits. Measuring the curvature of the computed χ^2 (Bevington, 1969) gives unreasonably large errors: The fits are obviously bad long before the 1-sigma uncertainties estimated from the curvature of χ^2, and differences in reduced χ^2 of 0.1 or even 0.05 are clearly significant. This is in part because many of the "degrees of freedom" are in fact additive background noise: If we limit the degrees of freedom to be those that contribute at least as much signal in the model images as the thermal noise level, we reduce the number of degrees of freedom by a factor of 5. We thus had to make subjective judgments about the uncertainties, combining numerical changes in χ^2 with subjective assessments of "good fits" based on visual comparisons of the data and synthetic images.

The initial goal of the 2005 radar observations was to determine the oblateness of Bennu. As the asteroid rotates, the points on the equator move across the radar images, but points at the rotation pole remain motionless (Green, 1968). As a result, the Z dimension of the asteroid is less well determined than the X- and Y-dimensions: "squeezing" the model in the Z direction does not change the radar images much. If the sub-Earth latitude changes significantly during the observations, a better estimate can be made, and the 2005 observations were scheduled to obtain the maximum possible sky motion. Nonetheless, the Z uncertainty remains larger than the rest. Because of this weakness, the model tends to leave the oblateness wherever it starts, even as it is changing the details of the shape. To test the sensitivity of the model to changes in the overall Z dimension, we ran a suite of spherical harmonic models where the objective function encouraged or discouraged flattening (oblateness). The result was that changes of 5% in oblateness do not strongly affect the objective function, and 10% is allowed for some poles within the uncertainty. A similar test was repeated using the final faceted model shape and varying the Z-axis scale factor, and the results were the same. This 10% diameter uncertainty adds about 50 m uncertainty to the determined Z-axis dimension, dominating the error in that parameter and affecting the uncertainties in volume and density. In the determination of the "best" shape, we have applied a slight bias to the objective function to prefer smaller Z axes if it did not noticeably affect the result. The largest Z-axis dimensions allowed are larger than the intermediate equatorial axis, which would be rotationally unstable and is therefore ruled out, but we retain the large uncertainty because the Z axis dimension is still much more poorly determined than the X and Y dimensions.

The overall size of the asteroid was tested in the same way. The size determination rests on the measurement of the range from the

leading edge of the target (the "front cap") to the terminator, and also by measuring the edge-to-edge Doppler broadening of the target. The former depends on the radar scattering function to some extent and the latter on the pole direction. The model was expanded or contracted equally in all dimensions, allowing the radar scattering function to float and using the nominal pole and a set of trial poles 5° away. An expansion or contraction of up to 2%, or 10 m, is within the uncertainty, and the best value was independent of the pole direction within those limits. Adding the flattening uncertainty of 50 m in quadrature gives a *Z*-axis uncertainty of 52 m that is completely dominated by the flattening uncertainty.

3.5. Surface features

The asteroid has a fairly smooth "spinning top" shape similar to that of binary asteroids such as 1999 KW_4 (Ostro et al., 2006) and other "spheroidal" asteroids such as 2008 EV5 (Busch et al., 2011), but with a less well-defined equatorial ridge. The shape appears fairly smooth at small scales, with some large-scale features. There is one 10–20 m boulder on the surface that appears in both 1999 and 2005 radar images, but no other small-scale surface features are evident down to the radar resolution of 7.5 m.

In order to better visualize the "boulder", which is visible in some of the raw radar images as it rotates over the terminator, the model resolution was improved to 5 m in the region around the feature in both the Northern and Southern hemispheres. There is a feature in the model in both hemispheres that could be the boulder (Fig. 6). Most likely, the north–south ambiguity intrinsic to radar data makes either location a possible source of the bright feature. By having the simulated images mark the echo from particular locations on the model, we can determine that the boulder is on the Southern hemisphere. With sufficient iteration, and by forcing the northern hemisphere to be smoother, we could eliminate the ambiguity, but this small (and well understood) artifact does not affect our results.

3.6. Slopes

Chesley et al. (2013) have used the existing optical astrometry and the radar astrometry described in Section 5 to determine that the orbit can only be fit if non-gravitational forces due to the Yarkovsky effect are included. From this result, they conclude that the density of Bennu must be 958 ± 130 kg m^{-3}. Slopes have been computed over the surface of Bennu for the nominal density of 1 g cm^{-3} and the extreme limits, 0.85 and 1.15 g cm^{-3}. Slope is defined as the angle between the total gravitational acceleration plus centripetal acceleration vector and the surface normal. For the gravitational acceleration we assume constant density throughout the body (see Scheeres, 2012 for details on the computation). We find distinctly different mean slopes and slope distributions for each case. The mean slope for the nominal case is 19°, for the lower density case is 24° and for the higher density case is 16°. The distribution of slopes between these cases is also quite distinct. Fig. 7 shows a histogram of slopes for the three different cases. Such large changes in slope distributions across these densities implies that the distribution of loose regolith (which is driven by surface slopes (Miyamoto et al., 2007)) will be sensitive to the actual density distribution at this body. These aspects of the shape model are currently being investigated.

4. Radar properties and comparison to other objects

4.1. Average radar properties

The radar cross-section σ of a target is defined as the cross-sectional area (πr^2) of a perfectly reflective smooth metal sphere, that is, a perfectly reflective isotropic scatterer, that reflects the same power as the target in the same viewing geometry. It has units of area. The radar albedo $\hat{\sigma}$ is a dimensionless quantity defined as the ratio of the backscatter reflectivity of a target to that of a perfectly reflective metal sphere of the same size as the target. The definition of "size" in this context is somewhat uncertain, but should probably refer to a sphere with the cross-sectional area of the body. However, the absolute calibration accuracy in radar reflectivity measurements is typically 25–50%, so this subtlety can usually be ignored. The circular polarization ratio μ_C is defined as the ratio SC/OC of echo power received in the two circular polarizations from a circularly-polarized transmitted signal: it would be very nearly 0 for a large (compared to the wavelength) smooth metal sphere and very nearly 1 for a surface that completely randomized the polarization of the incident radiation. Several of the uncertainties that contribute to the poor accuracy of reflectivity measurements (transmitted power, telescope gain (out and back) and absolute receiver sensitivity, each calibrated to 5–10% uncertainty) cancel in the polarization ratios, so a typical calibration accuracy for μ_C is 5%. For most known materials, pure water ice and E- and V-type asteroids being notable exceptions (Virkki et al., 2012), μ_C is a measure of wavelength-scale roughness within a meter or so of the surface, as it is caused by uncorrelated multiple scattering. For large spherical targets such as the Moon, it is empirically possible to quantify this roughness as an RMS slope, but for small irregular bodies other effects may dominate. Under some conditions, the OC radar albedo can be used to infer the bulk density of the near-surface material (see Section 4.3). The OC radar albedos and polarization ratios of Bennu are given in the table below, along with Itokawa, Eros, and 2005 YU_{55} for comparison, at both 12.6-cm and 3.5-cm wavelengths. The notable features are:

Bennu has a lower polarization ratio, and thus is probably smoother at wavelength scales, than any of these other asteroids. The spacecraft-imaged small body with the most similar polarization ratio is Phobos. The polarization ratio of Bennu is the same to within the uncertainties at both wavelengths; thus there are no dramatic textural changes occurring between these size scales. These values are global averages, and there may well be regional variations in surface properties.

Itokawa has a higher polarization ratio at 3.5 cm than at 12.6 cm, by a statistically significant factor of almost two. This difference suggests that the particle size distribution on Itokawa is changing at the few-cm scale, and would be consistent with the surface of Itokawa being deficient in particles smaller than about 3.5 cm compared to Bennu.

4.2. Polarization maps

The surface texture can in principle be studied by examining the polarization properties of the scattering. One property of interest is the circular polarization ratio μ_C which is generally a property of surface roughness, though modified by composition. When the radar images are acquired, we can sample both circular polarizations. This is generally done in the initial uncoded (CW) observations to obtain a global measure of the polarization ratio. In the imaging observations, it is possible to obtain images in either polarization as well.

We attempted to generate radar images of the polarization ratio by simply determining the image ratios on a pixel-by-pixel basis. However, on the days that the SC data have enough usable signal, the OC images are dominated by self-noise (see Section 3) in a way that varies with position on the asteroid. The polarization ratio thus has a denominator that is extremely variable (noisy), and the ratio images thus generated are meaningless.

We chose another approach to attempt to determine the radar scattering properties of the surface of Bennu. There are approximately 50 summed images from 1999 that go into generating the

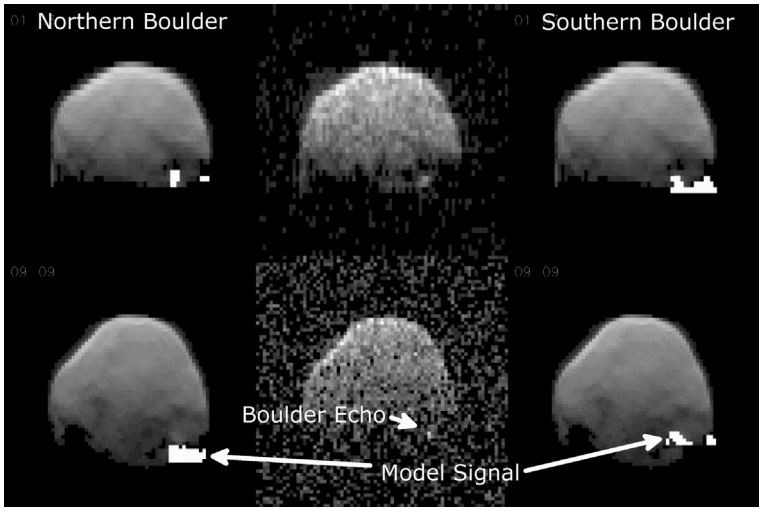

Fig. 6. Fits and data showing the boulder feature. The left column shows the fits with the boulder in the northern hemisphere and the right column has it in the south. The data are in the center. The top row is from 1999, and the bottom row is from 2005. The white marks show the computed location of the signal from the boulder. These white marks are very heavily stretched, and so look much larger than the actual feature. For both northern and southern boulders, the 1999 model overlaps the data. But for the 2005 geometry, the northern boulder is lower in the model image than in the data, while the southern boulder is in the same location in both the model image and the data. Therefore, the boulder is in the southern hemisphere.

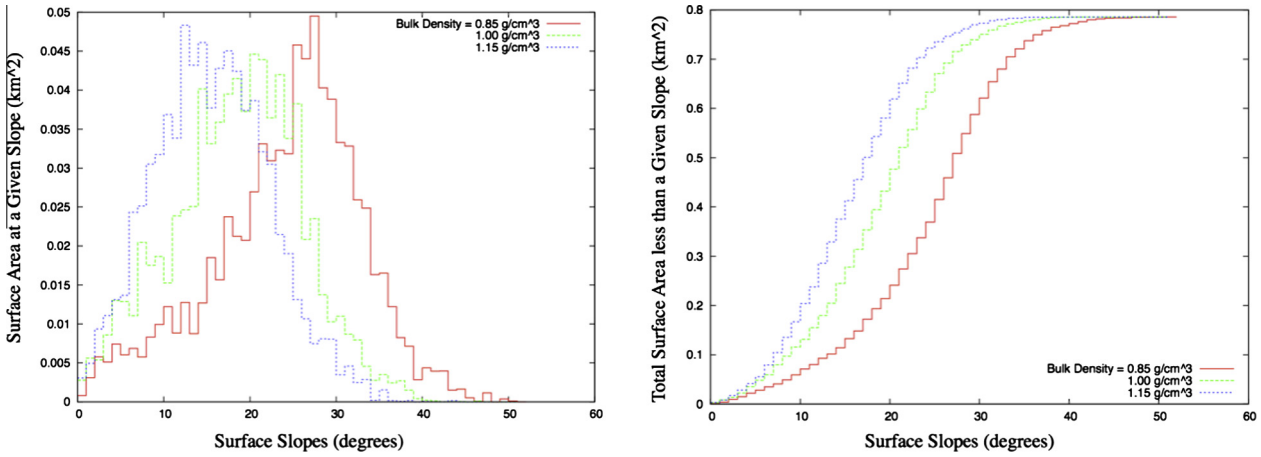

Fig. 7. Differential (left) and cumulative (right) distribution of facet-scale surface slopes vs. surface area for Bennu for the three different densities. Lower bulk densities yield higher slopes. The histogram is computed at a resolution of 1° of slope. The total surface area of the asteroid is 0.7855 km^2.

radar model, each with of order 100 pixels with signal. We used the shape model generated above, and refit the model allowing only the radar reflectivity to vary as a function of latitude and longitude, along with a single global angular dependence on incidence angle that was different for the two polarizations. As with the shape modeling, the scattering law used was of the form $R(C+1)\cos^{2C}\theta$, however the reflectivity R was allowed to be a function (spherical harmonics) of latitude and longitude, but C was a single constant for each polarization. This change was necessary as the OC echo is typically much more specular than the SC echo, and so purely geometric differences in scattering would dominate the latitude dependence. All other model parameters were held constant using the best-fit shape model. We separately fit the radar reflectivity of the model using the OC and the SC data.

Fig. 8 shows maps of the reflectivity R for the OC and SC models of Bennu using a spherical-harmonic reflectivity map of degree and order 4. Because of the complicated dependence of SNR on the details of the radar images, it would be possible for these maps to be dominated by noise. However, the maps show that the OC and SC reflectivities are correlated but not identical.

The north pole appears to be radar-brighter than the south pole in both polarizations. This effect could arise from a viewing geometry that favored one over the other, but the data used in this fit are all taken within about 20° of the equator, so that seems unlikely.

Also, the SC polarization is less reflective around the equator than the OC image, suggesting spatial variability of regolith roughness at the 10-cm scale of the radar wavelength, possibly with a smoother surface near the equator.

Higher-order maps show more differences, but these also appear more noise-like. It's likely that they represent real changes in surface properties, but this is difficult to demonstrate given the SNR and lack of features in the data. In order to check that these effects are not simply noise, the test was repeated twice using half of the data—the even- and odd-numbered images on each day. The results were similar but differed in some details, suggesting that the differences are real but that fine details may not be significant. Comparing these results with resolved images taken by the OSIRIS-REx spacecraft may clarify the relation between these maps and surface texture.

4.3. Near-surface bulk density

Radar scattering properties are related to composition, density, and material texture of the penetration depth of surface material, about 10 wavelengths for most rocks, ~meter-scale (e.g., Ostro et al., 2002). The details are complicated, but the most useful properties are that rough surfaces tend to depolarize an incident polarized ray due to multiple and irregular scattering, and that specular reflections, which preserve degree of polarization (though altering its direction), occur from changes in the index of refraction at a surface boundary, which is typically related to material density. Magri et al. (2001) used these properties to attempt to determine the bulk and grain densities of surface material of near-Earth asteroids using 433 Eros and L-chondrite meteorites as "ground truth". Magri et al. derive two relationships for density. The first, "uncalibrated" method extrapolated laboratory and planetary (Moon and Venus) scattering measurements to derive bulk density, and the second method simply assumes that Eros is a typical near-Earth asteroid and that bulk density scales linearly with the OC radar albedo. Because the textural and compositional properties of asteroids are not well known, Magri et al. make some assumptions about geometric and compositional factors.

For the "uncalibrated" determination, the relation is

$$d = 3.2\ \mathrm{g\ cm^{-3}} \ln\left[\frac{1+\sqrt{\frac{\sigma_{OC}}{g}\left(1-\frac{\mu_C}{\mu_{C,diff}}\right)}}{1-\sqrt{\frac{\sigma_{OC}}{g}\left(1-\frac{\mu_C}{\mu_{C,diff}}\right)}}\right],$$

where g is a geometric factor taken to be 1.2 and $\mu_{C,diff}$ is a correction for multiple scattering taken to be 0.5. Magri et al.'s Eq. (11) included an additional factor of $1/(1-p)$ to compute the grain density assuming a porosity p. Using a radar albedo $\sigma_{OC} = 0.12$ and circular polarization ratio $\mu_C = 0.18$ from Table 3, we get a bulk density of 1.65 g cm^{-3}. Alternatively, using Magri et al.'s linearized "Eros-calibrated" method, we obtain a grain density $\sigma_{OC,Bennu}/\sigma_{OC,Eros} = 0.12/0.25 = 1/2$ that of Eros. Magri et al. assume Eros to have L-chondrite composition, with a grain density of 3.75 g cm^{-3} and a porosity of about 50%, giving a bulk density of about 1.8 g cm^{-3} (for Eros), and thus grain/bulk densities of 1.8/0.9 g cm^{-3} for Bennu. These densities are not, a priori, unreasonable estimates for Bennu. Chesley et al. (2013), obtain an estimate of the bulk density of the entire asteroid to be ~1 g cm^{-3} from a measurement of the Yarkovsky effect on the orbit of Bennu, suggesting a fairly uniform porosity of about 0.5 for the entire asteroid, though the uncertainties are large enough to prevent drawing any firm conclusions. More recent studies of the densities of L-chondrites (Consolmagno et al., 2008) give slightly lower densities (by 5–10%), and the results should scale with that value.

5. Astrometry

The model explicitly fits the position of the center of mass of the asteroid in the image, which we use to improve the ephemeris. The datataking method ties the absolute distance to the object to the position in the radar images to about ±1/2–pixel precision. However, examining raw delay-Doppler images, it is not usually possible to identify the center of mass position in the images to that accuracy. The shape model can locate the center of mass (constrained in the shape modeling to be near the center of figure under an assumption of uniform density) to approximately the equatorial radius uncertainty, allowing us to estimate the center of mass distance from Bennu to the Arecibo telescope to approximately 15-m final precision, about 5 times better than was possible from the raw data. The assumption of uniform density contributed less than 0.01% of the reduced χ^2, so it is not possible to rule out that assumption using these data. Radar astrometric data are available from the Minor Planet Center or the JPL radar astrometry database http://ssd.jpl.nasa.gov/?radar. The astrometry consists of round-trip light travel times and Doppler shifts between the reference point of the observatory (the point at which the elevation and azimuth axes cross) and the center of figure of Bennu as determined from the shape model, for a signal that arrives at the

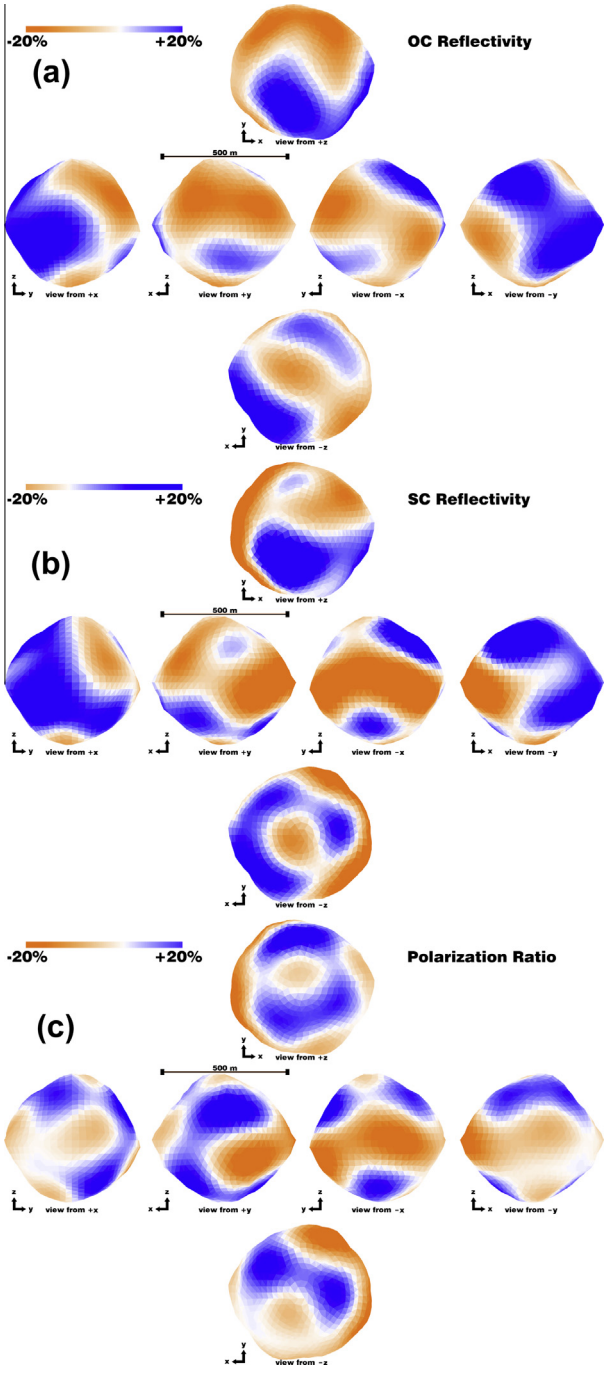

Fig. 8. OC (a), SC (b), and SC/OC ratio μ_C (c) maps of Bennu based on fitting the reflectivity of the surface to the 1999 data. The maps are 4th-order spherical harmonic fits to the data overlain on the shape model oriented as shown in Fig. 5. Orange is low and blue is high reflectivity/ratio, with scale bars showing + and − 20% from the mean. The standard deviations of all of the values are about 10%.

receiving telescope at the reference UTC time. The round-trip light travel times are determined to approximately 100 ns (15-m) precision, but are reported as having an accuracy of 0.5–1.0 μs (75–150 m) to allow for possible systematic errors.

6. Rapid rotation and the search for satellites

This object was first observed before the rapid rotation and spheroidal nature of primaries of NEA binary systems, probably by the YORP effect, was established (Margot et al., 2002; Pravec et al., 2006; Vokrouhlický et al., 2003). However, the rapid rotation rate suggested that a companion might be present. Searches in the 1999 data and again in 2005 reveal no companion bigger than 15 m, assuming a 1-min rotation period for the satellite, no larger than 5 m for satellites rotating with a 1-h period, and no more than 2 m for satellites rotating with a 24-h period. Most NEA binary systems now known (Pravec et al., 2006) have primaries rotating more rapidly than Bennu (typically 3 h or faster) so perhaps it is still being spun up, or it reached an obliquity that reduced or stopped the spin acceleration before it could become a binary system. Perhaps Bennu had a satellite in the past that has been lost. We could not measure any change in the rotation rate between 1999 and 2005, and cannot determine whether there is any current change in the rate in either direction. It is possible that future observations might do so, and the OSIRIS-REx mission certainly will if there is any.

7. Implications for OSIRIS-REx

This work clearly demonstrates that radar astronomy is a valuable tool for scientific investigation of asteroids. The extensive knowledge database that exists as a result of the radar characterization of Bennu was critical in the selection of this object as the OSIRIS-REx mission target. These data provided critical refinement of the asteroid's orbit and a substantial improvement of its ephemerides compared to optical astrometry. These data feed directly into the design of the overall OSIRIS-REx mission profile and constrain the launch period, the outbound and return cruise phases, and the timing and duration of asteroid proximity operations.

The radar-derived constraints on asteroid size and spin state also inform us about the nature of the asteroid environment. Radar astrometry has also revealed the action of the Yarkovsky effect (Chesley et al., 2013). This observation, when combined with the asteroid volume derived from the radar shape model and observational constraints on the thermal inertia of the body, allowed us to estimate the bulk density. Combining the derived density with the shape model provides the global asteroid gravity-field model, which allows the mission team to evaluate the stability of various orbits about the asteroid. The gravity-field model and the rotation state allowed us to develop a global surface-slope-distribution model and a global surface-acceleration model. These models are critical to evaluating our ability to safely deliver the spacecraft to the asteroid surface and maintain a nominal attitude during the 5-s touch-and-go sampling event. Finally, combining the asteroid shape, rotation state, ephemeris, and albedo yields a global temperature model, which is a direct input into the mission Environmental Requirements Document. All of this information feeds directly into the design of the OSIRIS-REx flight and ground systems, reducing risk and greatly increasing the chances for mission success.

Radar observations also provide constraints on the physical and chemical properties of the asteroid regolith. The observed smooth surface, radar albedo, polarization ratio, and shape all provide evidence of the presence of loose particulate regolith on the surface of this target. We interpret variations in radar albedo as variations in near-surface regolith density structure and metal content, but additional work is required to constrain the radar characteristics of likely regolith material. The circular polarization ratio likely reflects variations in regolith block content. The global shape model of the asteroid indicates a body symmetrically disposed about the rotational axis in response to centrifugal forces. This result suggests that there is loose material capable of migrating into geopotential lows. Our global surface-slope-distribution model has a subdued slope distribution at the spatial resolution of the shape model (7.5 m/pixel). The average slope is 15–24°, depending on the bulk density of the asteroid. The geopotential low of the asteroid is at the equator (Guibout and Scheeres, 2003), suggesting that

Table 3
Overall radar scattering properties of Bennu and other radar-observed small bodies that have been visited by spacecraft. If a reference is listed with the name of an object, it applies to all of the data columns for that object. All other values were measured by the authors using standard techniques from archival data. The uncalibrated and Eros-calibrated near-surface bulk densities are computed from the 12.6-cm OC albedo and polarization ratio using the method of Magri et al. (2001), Eq. (11), except that the porosity factor $1/(1-p)$ has been excluded; thus these are bulk densities rather than solid densities. Similarly, the "Eros-calibrated" near-surface bulk density has been calculated using the assumption that Eros has a near-surface bulk density of 3.75/2 = 1.875, i.e., half that of L-chondrite meteorites, and that near-surface bulk density scales with OC radar albedo, as in Magri et al., but with no attempt to adjust for porosity.

	12.6-cm polarization ratio, μ_C = SC/OC	3.5-cm polarization ratio, μ_C = SC/OC	12.6-cm OC radar albedo	"Uncalibrated" near-surface bulk density	"Eros-calibrated" near-surface bulk density
Bennu	0.18 ± 0.03	0.19 ± 0.03	0.12 ± 0.04	1.66	0.90
Itokawa	0.26 ± 0.04[a]	0.47 ± 0.04	0.14 ± 0.04[a]	1.54	1.05
Eros[b]	0.28 ± 0.06	0.33 ± 0.07	0.25 ± 0.09	2.00	1.88
2005 YU_{55}	0.41 ± 0.08[c]	0.36 ± 0.05	0.18 ± 0.05	1.06	1.35
Lutetia[d]	0.22 ± 0.07		0.17 ± 0.07	1.85	1.28
Mathilde	0.08 ± 0.04		0.071 ± 0.02	1.45	0.53
Phobos[e]	0.17 ± 0.04		0.06 ± 0.014	1.18	0.45
Deimos[e]	0.12 ± 0.12		0.021 ± 0.006	0.74	0.16
103P/Hartley 2[f]	0.37 ± 0.04		0.041 ± 0.010	0.61	0.31
4 Vesta[g]	0.24 ± 0.06	0.32 ± 0.04	0.08 ± 0.03	1.21	0.60
4179 Toutatis[h]	0.23 ± 0.03	0.29 ± 0.01	0.21 ± 0.03	1.80	1.70

[a] Ostro et al. (2004).
[b] Magri et al. (2001).
[c] Value is standard deviation of 9 days of observation, not uncertainty.
[d] Magri et al. (1999).
[e] Busch et al. (2007).
[f] Harmon et al. (2011). No uncertainties reported, but assumed to be typical for the Arecibo radar system.
[g] Mitchell et al. (1998).
[h] 12.6 cm μ_C is from archival Arecibo data from 2004. All other values are from Magri et al. (2001), and are at 3.5 cm, not 12.6 cm.

loose regolith should migrate down to this region, such as has occurred on Itokawa (Miyamoto et al., 2007). If sufficient migration has occurred, the gravels would build up a structure at the equator, a likely origin for the observed equatorial ridge on Bennu.

Analysis of the OSIRIS-REx returned sample will improve the interpretation of remote sensing data, including radar astronomy data, but also spectroscopy and scattering properties at all wavelengths. Sample analysis has the potential to address two key questions for asteroid regoliths: (1) What is the effect of compositional variations in mineral constituents (e.g., pyroxenes) on dielectric properties? and (2) What is the effect of adsorbed H_2O on dielectric properties? Asteroid regolith materials likely have very low dielectric losses, so small variations in secondary components may have a profound effect, as could textural density differences (Campbell and Ulrichs, 1969). A better understanding of these variations will improve our ability to make robust interpretations of other radar observations. We will analyze the returned material to develop a body of knowledge about the dielectric properties of good analogs that will enable us to place Bennu samples in the appropriate context. We will also use knowledge about Bennu regolith from returned samples to understand variations in radar properties of other objects. Thus, radar astronomy of the OSIRIS-REx target asteroid has facilitated efficient mission planning and science objective planning and sample return from this object will provide enormous benefit to future radar studies of near-Earth objects.

8. Conclusions

The best-fit shape and pole position of Bennu have been derived from radar images combined with lightcurve data. The independent rotation rate determined from the lightcurve greatly increases the information we can gain from radar images. Modeling of pole orientation of Bennu was complicated by the ridged shape characteristic of this object, which dominates its equatorial width. Using a too-simple ellipsoidal shape gave misleading results because the radar data emphasize the (apparent projected) equatorial diameter. Similar issues may affect pole determination by other methods, as the dependence of the visible area on viewing geometry does not follow a simple pattern. Bennu has a retrograde rotation direction with a rotation pole at ecliptic coordinates $-88°, 45 \pm 4°$. This is consistent with it having been driven to a stable state by YORP (Vokrouhlický et al., 2003). The shape model derived is similar to that of the primary of 1999 KW_4 (Ostro et al., 2006). However, searches for a satellite for Bennu show nothing larger than 15 m. Radar observations are quite sensitive to satellites in NEAs, and are largely independent of viewing geometry or distance. The small size and spheroidal shape of this object suggests that it has a rubble-pile structure with little or no internal strength (Nolan et al., 2005). This is not unusual among NEAs observed with radar, but it is not universal. Objects of similar size are also seen which must have internal strength to maintain surface material at their spin rate (Taylor et al., 2012). The OSIRIS-REx spacecraft mission to this object will reveal new insights into the formation and evolution of near-Earth asteroids, and possibly give clues to their origins in the main belt as well. Radar observations of NEAs in general also gives invaluable information as to their sizes, shapes and diversity, and as a by product, gives greatly improved orbits for any object observed.

Acknowledgments

We thank Yu. Krugly for providing the original lightcurve data from 1999 for modeling. The Arecibo Observatory is part of the National Astronomy and Ionosphere Center, which at the time of observation was operated by Cornell University for the National Science Foundation. MCN and ESH were supported by NNX10AP64G, NNX12AF24G and funding from the OSIRIS-REx project, NNM10AA11C. CM was partially supported by NSF Grant AST-0205975. Some of this work was performed at the Jet Propulsion Laboratory (JPL), California Institute of Technology, under contract with the National Aeronautics and Space Administration (NASA). This material is based in part upon work supported by NASA under the Science Mission Directorate Research and Analysis Programs.

Appendix A. Supplementary material

Supplementary data associated with this article can be found, in the online version, at http://dx.doi.org/10.1016/j.icarus.2013.05.028.

References

Benner, L.A.M., Ostro, S.J., Magri, C., Nolan, M.C., Howell, E.S., Giorgini, J.D., Jurgens, R.F., Margot, J.L., Taylor, P.A., Busch, M.W., Shepard, M.K., 2008. Near-Earth asteroid surface roughness depends on compositional class. Icarus 198, 294–304. http://dx.doi.org/10.1016/j.icarus.2008.06.010.

Bevington, P.R., 1969. Data Reduction and Error Analysis for the Physical Sciences. McGraw-Hill, New York.

Busch, M.W., Ostro, S.J., Benner, L.A.M., Giorgini, J.D., Magri, C., Howell, E.S., Nolan, M.C., Hine, A.A., Campbell, D.B., Shapiro, I.I., Chandler, J.F., 2007. Arecibo radar observations of Phobos and Deimos. Icarus 186, 581–584.

Busch, M.W. et al., 2011. Radar observations and the shape of near-Earth Asteroid 2008 EV5. Icarus 212, 649–660. http://dx.doi.org/10.1016/j.icarus.2011.01.013.

Campbell, M.J., Ulrichs, J., 1969. Electrical properties of rocks and their significance for lunar radar observations. J. Geophys. Res. 74, 5867–5881. http://dx.doi.org/10.1029/JB074i025p05867.

Campins, H., Morbidelli, A., Tsiganis, K., de León, J., Licandro, J., Lauretta, D., 2010. The origin of Asteroid 101955 (1999 RQ36). Astrophys. J. 721 (1), L53–L57.

Chesley et al., 2013. Orbit and bulk density of the OSIRIS-REx target asteroid (101955) Bennu. Icarus, submitted for publication..

Clark, B.E. et al., 2011. Asteroid (101955) 1999 RQ36: Spectroscopy from 0.4 to 2.4 μm and meteorite analogs. Icarus 216 (2), 462–475.

Consolmagno, G.J., Britt, D.T., Mackey, R.J., 2008. The significance of meteorite density and porosity. Chem. Erde 68, 1–29.

Elachi, C., 1987. Introduction to the Physics and Techniques of Remote Sensing. Wiley, Section 6-3-6.

Green, P., 1968. Radar measurements. In: Evans, J.V., Hagfors, T. (Eds.), Radar Astronomy. McGraw-Hill, New York, Section 1-5E.

Guibout, V., Scheeres, D.J., 2003. Stability of surface motion on a rotating ellipsoid. Celest. Mech. Dynam. Astron. 87, 263–290.

Harmon, J.K., Nolan, M.C., Howell, E.S., Giorgini, J.D., Taylor, P.A., 2011. Radar observations of Comet 103P/Hartley 2. Ap. J. 734, L2, 1–4. http://dx.doi.org/10.1088/2041-8205/734/1/L2.

Hergenrother, C.W. et al., 2013. Lightcurve, phase and color photometry of the OSIRIS-REx target Asteroid (101955) Bennu. Icarus 226, 663–670.

Hudson, R.S.,1993. Three-dimensional reconstruction of asteroids from radar observations. Remote Sensing Reviews 8, 195-203. http://dx.doi.org/10.1080/02757259309532195.

Krugly, Yu.N., Belskaya, I.N., Shevchenko, V.G., Chiorny, V.G., Velichko, F.P., Mottola, S., Erikson, A., Hahn, G., Nathues, A., Neukum, G., Gaftonyuk, N.M., Dotto, E., 2002. The near-Earth objects follow-up program: IV. CCD photometry in 1996–1999. Icarus 158, 294–304. http://dx.doi.org/10.1006/icar.2002.6884.

Magnusson, P. et al., 1989. Determination of pole orientations and shapes of asteroids. In: Binzel, R.P., Gehrels, T., Matthews, M.S. (Eds.), Asteroids II. U. of Arizona Press, Tucson, pp. 66–97.

Magri, C., Ostro, S.J., Rosema, K.D., Thomas, M.L., Mitchell, D.L., Campbell, D.B., Chandler, J.F., Shapiro, I.I., Giorgini, J.D., Yeomans, D.K., 1999. Mainbelt asteroids: Results of Arecibo and Goldstone radar observations of 37 objects during 1980–1995. Icarus 140, 379–407.

Magri, C., Consolmagno, G.J., Ostro, S.J., Benner, L.A.M., Beeney, B.R., 2001. Radar constraints on asteroid regolith compositions using 433 Eros as ground truth. Meteorit. Planet. Sci. 36 (12), 1697–1709. http://dx.doi.org/10.1111/j.1945-5100.2001.tb01857.

Magri, C., Ostro, S.J., Scheeres, D.J., Nolan, M.C., Giorgini, J.D., Benner, L.A.M., Margot, J.L., 2007. Radar observations and a physical model of Asteroid 1580 Betulia. Icarus 186, 152–177.

Margot, J.L. et al., 2002. Binary asteroids in the near-Earth object population. Science 296, 1445–1448. http://dx.doi.org/10.1126/science.1072094.

Milani, A., Chesley, S.R., Sansaturio, M.E., Bernardi, F., Valsecchi, G.B., Arratia, O., 2009. Long term impact risk for (101955) 1999 RQ_{36}. Icarus 203 (2), 460–471.

Mitchell, D.L., Ostro, S.J., Hudson, R.S., Rosema, K.D., Campbell, D.B., Vélez, R., Chandler, J.F., Shapiro, I.I., Giorgini, J.D., Yeomans, D.K., 1996. Radar observations of asteroids 1 Ceres, 2 Pallas, and 4 Vesta. Icarus 124, 113–133. http://dx.doi.org/10.1006/icar.1996.0193.

Miyamoto, H. et al., 2007. Regolith migration and sorting on asteroid Itokawa. Science 316, 1011–1014.

Mitchell, D.L., Hudson, R.S., Ostro, S.J., Rosema, K.D., 1998. Shape of asteroid 433 Eros from inversion of Goldstone radar Doppler spectra. Icarus 131, 4–14. http://dx.doi.org/10.1006/icar.1997.5815.

Nolan, M.C., Hine, A.A., Howell, E.S., Benner, L.A.M., Giorgini, J.D., Ostro, S.J., Black, G.J., Campbell, D.B., Margot, J.L., Carter, L.M., Magri, C., 2005. Extreme diversity of near-Earth asteroid physical properties from Arecibo radar imaging. Bull. Amer. Astron. Soc. 37, 1155.

Ostro, S.J., Hudson, R.S., Benner, L.A.M., Giorgini, J.D., Magri, C., Margot, J.L., Nolan, M.C., 2002. Asteroid Radar Astronomy. In: Bottke, W.F., Cellino, A., Paolicchi, P., Binzel, R.P. (Eds.), Asteroids III. University of Arizona Press, Tucson, USA, pp. 151–168.

Ostro, S.J. et al., 2004. Radar observations of Asteroid 25143 Itokawa (1998 SF_{36}). Meteorit. Planet. Sci. 39, 407–424.

Ostro, S.J. et al., 2006. Radar imaging of binary near-Earth Asteroid (66391) 1999 KW_4. Science 314, 1276–1280. http://dx.doi.org/10.1126/science.1133622.

Pravec, P. et al., 2006. Photometric survey of binary near-Earth asteroids. Icarus 181, 63–93. http://dx.doi.org/10.1016/j.icarus.2005.10.014.

Scheeres, D.J., 2012. Orbital Motion in Strongly Perturbed Environments: Applications to Asteroid, Comet and Planetary Satellite Orbiters. Springer-Praxis, London, UK.

Taylor, P.A., Howell, E.S., Nolan, M.C., Thane, A.A., 2012. The shape and spin distributions of near-Earth asteroids observed with the Arecibo radar system. Paper presented at Asteroids, Comets, Meteors 2012, Niigata, Japan. Abstract #6340.

Ulabi, F.T., Moore, R.K., Fung, A.K., 1982. Microwave Remote Sensing, Active and Passive, vol. 2. Artech House, Norwood, Massachusetts, Section 7-2.2.

Virkki, A., Muinonen, K., Penttilä, A., 2012. Circular-Polarization Ratios and Radar Albedos: Interpretation in Terms of Near-Surface Physical Properties of Asteroids. Asteroids, Comets, Meteors, 2012. Abstract 6064.

Vokrouhlický, D., Nesvorný, D., Bottke, W.F., 2003. The vector alignment of asteroid spins by thermal torques. Nature 425, 147–151.

Walsh, K.J., Delbó, M., Bottke, W.F., Vokrouhlický, D., Lauretta, D.S., 2013. Introducing the Eulalia and new Polana asteroid families: re assessing primitive asteroid families in the inner Main Belt. Icarus 225, 283–297. http://dx.doi.org/10.1016/j.icarus.2013.03.005.